Plasmonic Slot Waveguide Propagation Analysis

Amrita Pati[1] and Reuven Gordon[1*]

[1]Department of Electrical and Computer Engineering, University of Victoria, 3800 Finnerty Road, Victoria, V8P 5C2, British Columbia, Canada.

*Corresponding author(s). E-mail(s): rgordon@uvic.ca;
Contributing authors: amritapati@uvic.ca;

Abstract

Plasmonic slot waveguides provide extreme light confinement with the benefits of having naturally present electrodes for switching and high thermal conductivity of the metal layers to remove excess heat. Past works relied on numerical computation for these structures, which is time-consuming and lacks physical insight. Here we present an analytical model of plasmonic slot waveguides to determine the modal properties based on single-mode matching to continuum. The model is accurate to within 3% of rigorous numerical simulations. The theory allows for rapid design and provides physical insight into mode propagation in plasmonic slot waveguides for information processing, optical manipulation, and sensing applications.

Keywords: plasmonic slot waveguides, modulators, optical sensing, optical trapping, and manipulation

1 Introduction

Plasmonic slot waveguides support extremely localized electromagnetic modes over a wide range of frequencies [1–3]. They have been applied in high-speed information processing applications [4–13], optical tweezers [14, 15], extreme confinement for light-matter interactions, and sensing [16, 17]. The waveguides sustain modes with long propagation lengths in the optical communication

regime [3, 18], allow sharp bending at lower scattering losses compared to their dielectric counterparts [19], and are easy to fabricate. They allow electrical bias fields and optical modes in the same region, which favors integration with existing electronics [20]. The two metal layers provide electrical contacts down to the nanometer scale [21, 22], while their high thermal conductivity facilitates heat removal from the circuitry [13, 23, 24]. They merge the subwavelength operation of electronics with the large bandwidth of photonics, promising a new generation of faster and ultra-compact photonic integrated circuits [4, 11, 25–29].

A careful analysis of the slot waveguide geometry is required to optimize structural parameters for different applications. The trade-off between mode confinement and propagation length is a common challenge. Other design challenges include achieving high sensitivity in sensing applications and optimizing electronic response times (i.e., managing capacitance). Past works used numerical methods to study these geometries and the modes supported by them [1–3, 18, 19, 30]. Although accurate, numerical simulations do not provide physical insight and are resource intensive. For each parameter variation, a new calculation is required to determine the propagation properties. Analytical models compute physical parameters like reflection phase, which can be used in the accurate design and have been applied to other plasmonic geometries [31–48].

We present a fully analytic theory to determine the properties of modes found in plasmonic slot waveguides. An analytic expression of the reflection coefficient at the slot-dielectric interface is derived by combining single-mode matching to continuum with an approximate mode shape. The reflection phase values obtained from this equation are used in the transverse resonance waveguiding condition in the geometric optics framework to calculate the mode effective index and propagation length. The results are shown to be accurate by numerical simulations performed with commercially available numerical software. The analytic approach allows for rapid calculation of the propagation properties and provides physical insight into the design space. Compared to a past work that used the effective index method as an analytic approach, here we include a more accurate formulation of the phase of reflection that incorporates the mode-shape mismatch at the boundary [49]. The approach is useful for the efficient design and optimization of plasmonic slot waveguides in applications ranging from information processing to sensing.

2 Reflection in the Plasmonic Slot Waveguide

Figure 1a shows a schematic of the slot waveguide geometry under consideration. Two gold films of thickness l and permittivity ϵ_m (values taken from a past work [50]) are separated by a distance of a. They are surrounded by dielectric media of permittivity ϵ_{d1} at the top ($z = l/2$), ϵ_{d2} at the bottom ($z = -l/2$), and ϵ_d inside the slot. The gap plasmon mode in the slot is quasi-TEM (transverse electromagnetic). The transverse electric field along

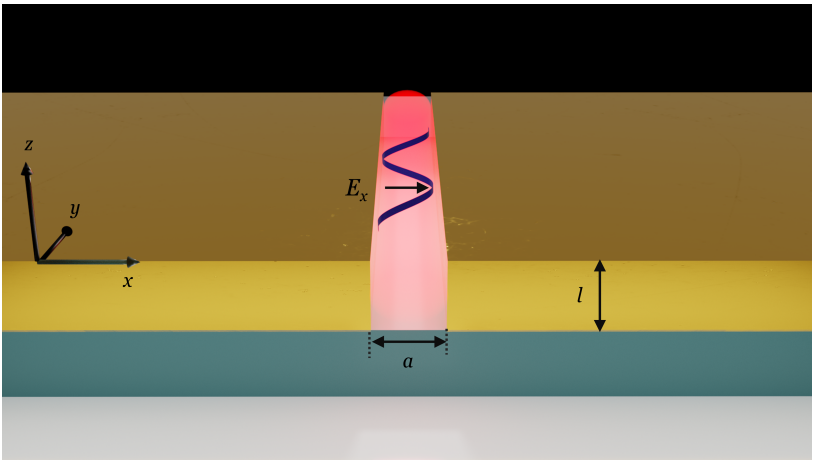

(a)

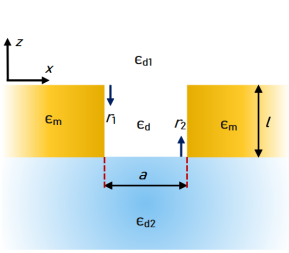

(b)

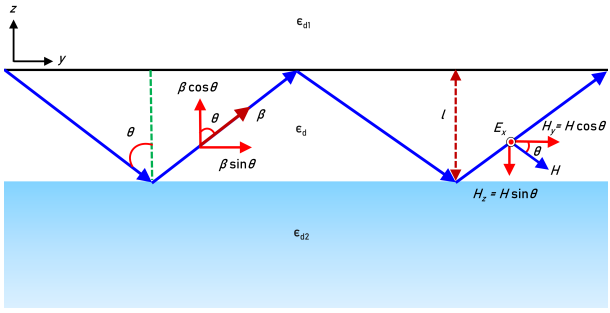

(c)

Fig. 1 (a) Schematics of the 3D plasmonic slot waveguide of width a and metal thickness l surrounded by different dielectric media. (b) $x - z$ view of the waveguide showing the reflection coefficients r_1 and r_2. (c) $y - z$ view of the waveguide, showing the total internal reflection of the gap plasmon mode.

the $x-$direction is represented by E_x. Propagation takes place in the $y - z$ plane, making an angle θ with the $z-$axis. The magnetic field (H), being perpendicular to the propagation direction is also directed in the y (H_y) and z (H_z) directions as shown in Figure 1c. When θ exceeds the critical angle (θ_c), the gap plasmon mode propagates by total internal reflection at the slot-dielectric interfaces. The two reflection coefficients r_1 and r_2 are shown in Figure 1b. All subsequent calculations are performed at a wavelength (λ) of 1550 nm.

2.1 Effective Index Approximation

Our analysis is based on a combination of perfect electric conductor (PEC) approximation and dielectric loading, which has been previously shown to be

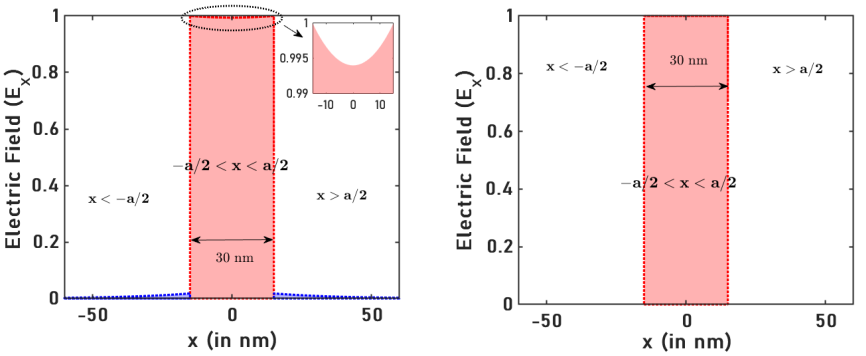

Fig. 2 (a) The exact values of E_x (normalized to its maximum value) inside and outside a slit (MIM geometry) of width 30 nm at a wavelength of 1550 nm (b) E_x approximated by a rectangle function of amplitude 1 for the analysis presented here.

accurate for 2D slits [51]. The effectiveness of this approach is explained by two key observations. The hyperbolic cosine dependence of the transverse electric field inside the slot on the position (x) becomes almost constant in the limit $a << \lambda$.

Secondly, the continuity of the normal component of the electric displacement field (D_x) across each metal-dielectric interface (at $x = -a/2$ and $x = a/2$) gives the ratio of E_x in the metal and the slot as ϵ_d/ϵ_m. The large values of ϵ_m at long wavelengths cause E_x to be significantly lower in the metal relative to the slot as shown in Figure 2a. This enables us to approximate the overall electric field by a rectangle function, shown in Figure 2b, with unit amplitude for $|x| < a/2$ and 0 otherwise.

Dielectric loading is introduced as a means of including the finite conductivity and absorption of real metal. The slot is replaced by a material of complex refractive index n_{MIM}, which is the effective index of a gap plasmon mode given by β/k_0. k_0 is the free-space wave vector and β is the propagation constant in a metal-insulator-metal (MIM) structure calculated by solving the following dispersion relation:

$$\tanh\left(\sqrt{\beta^2 - \epsilon_d k_0^2}\,\frac{a}{2}\right) = -\frac{\epsilon_d}{\epsilon_m}\frac{\sqrt{\beta^2 - \epsilon_m k_0^2}}{\sqrt{\beta^2 - \epsilon_d k_0^2}} \tag{1}$$

2.2 Single Mode-Matching to Continuum

The single-mode matching to continuum method is used to derive an analytic expression for reflection coefficients, r_1 and r_2. In the subwavelength regime ($a << \lambda$), it is a good approximation to assume that only a single mode can be localized in the $x-$direction inside the slot. The transverse electric and magnetic fields of this mode are matched with the corresponding fields of the continuum of modes outside the slot under PEC approximation.

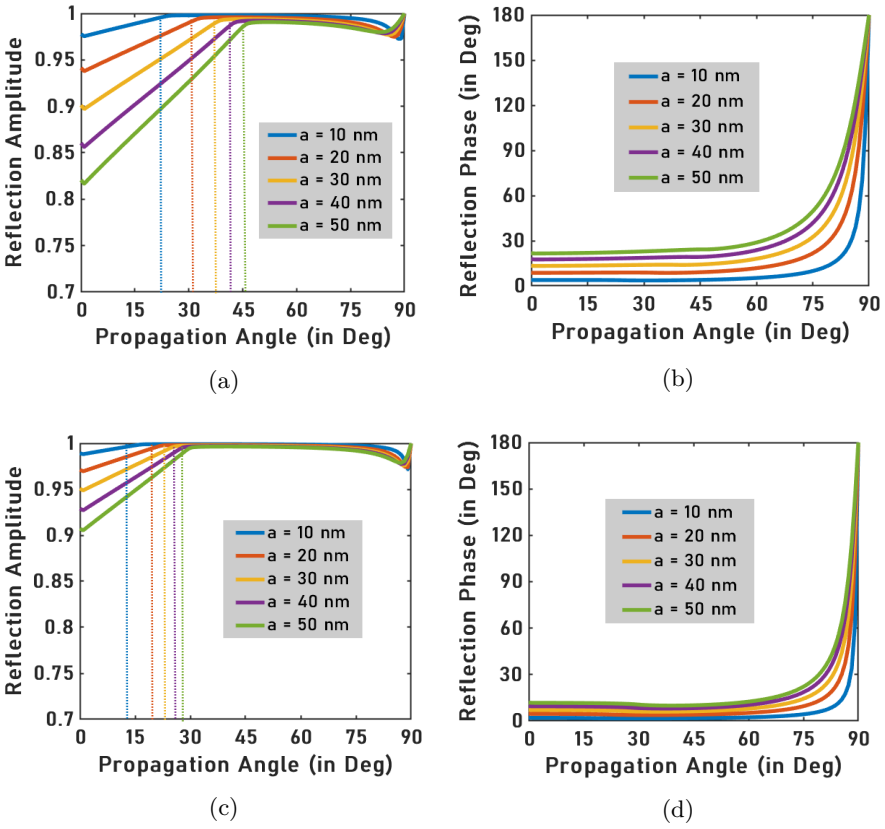

Fig. 3 (a) Reflection amplitude and (b) reflection phase of the gap-plasmon mode in a plasmonic slot waveguide completely surrounded by silica (SiO_2) of refractive index 1.44, $\epsilon_d = \epsilon_{d1} = 2.0736$. (c) Reflection amplitude and (d) phase for SiO_2 inside the slot and air outside it for widths of 10 nm to 50 nm at a wavelength of 1550 nm. Vertical dotted lines indicate the critical angles.

Considering the interface at the top, the electric field in the slot is given by:

$$E_x(z = 0^-) = (1 + r_1)\text{rect}\left(\frac{x}{a}\right)\exp\left(ik_y.y\right) \tag{2}$$

Here, $\text{rect}(x/a)$ is the rectangle function whose value is 1 for $-a/2 < x < a/2$ and 0 everywhere else. The electric field just above the slot interface is given as:

$$E_x(z = 0^+) = \int_{-\infty}^{\infty} t(k_x)\exp\left(ik_y.y + ik_x.x\right)\, dk_x \tag{3}$$

By matching these fields at the boundary ($z = 0$) and using the orthogonality of modes, we obtain the relationship between r_1 and the transmission

coefficient $t(u)$ as follows:

$$t(u) = \lambda \frac{(1+r_1)}{\pi u} \sin\left(\frac{\pi a u}{\lambda}\right) \tag{4}$$

where, $u = k_x/k_0$. Similarly, the transverse component of the magnetic field (H_y) inside the slot is given as:

$$H_y(z=0^-) = \frac{\omega\sqrt{\epsilon}_d}{k_0}(1-r_1)\text{rect}\left(\frac{x}{a}\right)\exp\left(ik_y.y\right)\cos\theta \tag{5}$$

and just above the slot is given as:

$$H_y(z=0^+) = \omega\epsilon_{d1}\int_{-\infty}^{\infty} t(k_x)\frac{\sqrt{\epsilon_{d1}k_0^2 - \epsilon_d k_0^2\sin^2\theta - k_x^2}}{\epsilon_{d1}k_0^2 - k_x^2}\exp(ik_x.x + ik_y.y)\,dk_x \tag{6}$$

On replacing k_x by uk_0, substituting the value of $t(u)$ obtained from Eq. 4, and applying orthogonality condition to the matched transverse magnetic fields, we obtain r_1 as:

$$r_1 = \frac{\sqrt{\frac{\epsilon_d}{\epsilon_{d1}}}\cos\theta - I_1}{\sqrt{\frac{\epsilon_d}{\epsilon_{d1}}}\cos\theta + I_1} \tag{7}$$

where, I_1 is:

$$I_1 = \int_{-\infty}^{\infty} \frac{\sqrt{1 - \frac{\epsilon_d}{\epsilon_{d1}}\sin^2\theta - \frac{u^2}{\epsilon_{d1}}}}{1 - \frac{u^2}{\epsilon_{d1}}}\frac{\sin^2(\pi u w)}{\pi^2 u^2 w}\,du \tag{8}$$

and $w = \dfrac{a}{\lambda}$. The same steps are used to derive an expression for the reflection coefficient at the bottom of the slot (r_2), the only difference in the resulting equation was that ϵ_{d1} is replaced by ϵ_{d2}.

For the case of a real metal, ϵ_d is replaced by n_{MIM}^2 resulting in new values of r_1 and I_1 as:

$$r_1 = \frac{\sqrt{\frac{n_{\text{MIM}}^2}{\epsilon_{d1}}}\cos\theta - I_1}{\sqrt{\frac{n_{\text{MIM}}^2}{\epsilon_{d1}}}\cos\theta + I_1} \tag{9}$$

and:

$$I_1 = \int_{-\infty}^{\infty} \frac{\sqrt{1 - \frac{n_{\mathrm{MIM}}^2}{\epsilon_{d1}} \sin^2\theta - \frac{u^2}{\epsilon_{d1}}}}{1 - \frac{u^2}{\epsilon_{d1}}} \frac{\sin^2(\pi u w)}{\pi^2 u^2 w}\, du \tag{10}$$

Figure 3a shows the variation of reflection amplitude with the propagation angle for different slot widths. The material above and below the interface is (SiO_2) of refractive index 1.44 ($\epsilon_d = \epsilon_{d1}$). The reflection amplitudes are higher for narrower slots due to increased penetration of the electric fields into the metal. When the angle exceeds the critical angle, given by $\sin^{-1}[\sqrt{\epsilon_{d1}}/n_{\mathrm{MIM}}]$ and indicated by the vertical dotted lines, total internal reflection takes place but the reflection amplitude is slightly less than 1 due to metal absorption. Narrower gaps have lower critical angles due to a higher difference between refractive indices inside and outside the slot. The reflection phase shown in Figure 3b increases with θ and the slot width but reaches π for $\theta = \pi/2$ regardless of the gap widths.

Figure 3c shows the reflection amplitude for a slot interface with SiO_2 inside and air outside ($\epsilon_d \neq \epsilon_{d1}$). The values of reflection amplitude for corresponding widths are slightly greater compared to those in Figure 3a. This is due to the increased contrast between the index of the gap plasmon inside the slot and that of air outside as opposed to SiO_2, which also results in lower values of critical angles. The reflection phases in Figure 3d are similar in their overall trend to Figure 3b but they appear more squeezed together due to their lower values also resulting from the higher contrast.

3 Geometric Optics Approach

The solutions for propagation angles of the plasmonic slot waveguide are calculated from the transverse resonance condition also known as the self-consistency condition. This approach has been previously used to determine the properties of plasmonic stripe waveguide [41]. For a waveguide to sustain a bound mode, the total phase acquired in a roundtrip must be integral multiples of 2π, written as:

$$2 \times \Re(\beta) \times l \cos\theta_m - \phi_1 - \phi_2 = 2m\pi \tag{11}$$

m is an integer and ϕ_1 and ϕ_2 are the reflection phases at the top and bottom interfaces of the slot. $\Re(\beta)$ is the real part of the complex propagation constant in the MIM. The values of θ_m that satisfy Eq. 11 for different values of m are used in the following equation to calculate the mode effective indices ($n_{m,\mathrm{mode}}$) for the fundamental and higher order modes:

$$n_{m,\mathrm{mode}} = n_{\mathrm{MIM}} \sin\theta_m \tag{12}$$

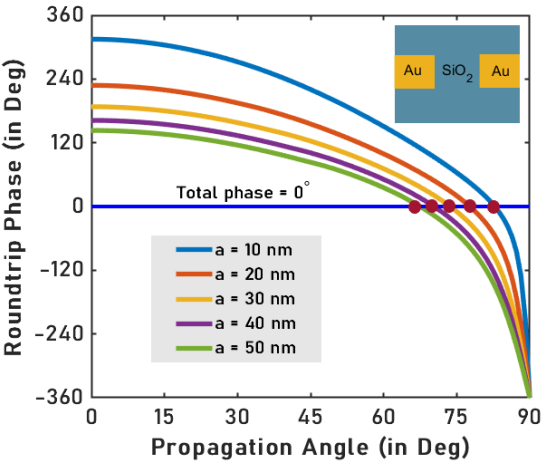

Fig. 4 Total roundtrip phase of the EM waves in the symmetric waveguide completely surrounded by SiO_2 for slot widths of 10 nm to 50 nm and metal thickness of 200 nm. Horizontal blue line represents a total phase of 0 and the red circles are fundamental mode solutions.

For all our subsequent calculations we use two configurations of plasmonic slot waveguides: symmetric and asymmetric. For the symmetric case, the two gold films are completely surrounded by SiO_2 ($\epsilon_{d1} = \epsilon_d = \epsilon_{d2}$) and therefore $r_1 = r_2$. The asymmetric waveguide has air above the top interface and SiO_2 inside the slot and as the substrate ($\epsilon_{d1} \neq \epsilon_d = \epsilon_{d2}$) implying $r_1 \neq r_2$.

3.1 Symmetric Waveguide

Figure 4 shows the total roundtrip phase of the gap plasmon mode in the symmetric configuration for slot widths ranging from 10 nm to 50 nm and film thickness of 200 nm. This is calculated from the left-hand side of Eq. 11 by using $\phi_1 = \phi_2$. The horizontal blue solid line corresponds to a phase of 0. Its intersections with the total phase curves, denoted by the red circles are fundamental mode solutions of the symmetric waveguide.

Figure 5a shows the variation of the fundamental mode effective index and propagation length with the slot width of the symmetric waveguide. The effective index increases with a decrease in the slot width similar to a 2D slit due to the increasing amount of electric field entering the metal. As $a \to 0$, the effective index approaches n_{MIM}, since the fundamental order solution $\theta \to 90°$. These observations are also verified using results from numerical simulations shown by purple squares. Simulations are performed by solving the mode source in ANSYS Lumerical FDTD v2020 R2.3 within perfectly matched layer boundaries. A uniform mesh size of 0.1 nm is used inside the slot and 1 nm is used for the rest of the simulation region. Au (Gold) - Johnson and Christy is chosen from the Material Database to form the gold layers and a user-defined index of 1.44 is used for silica. The red solid line in Figure 5a

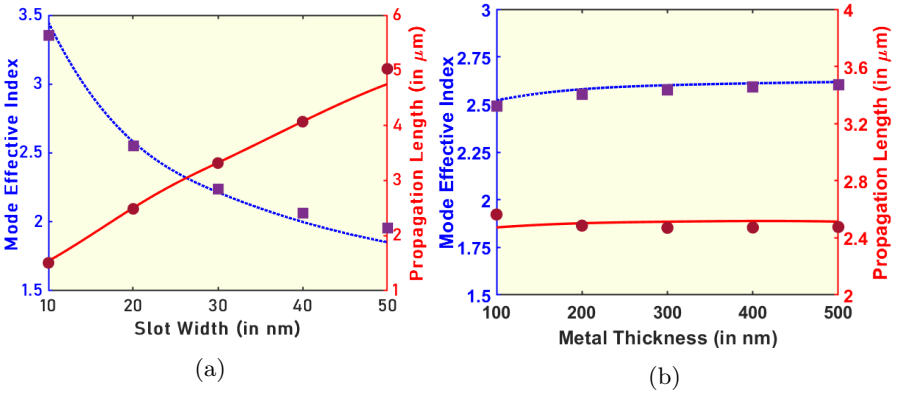

Fig. 5 Variation of the fundamental mode effective index (the blue dotted line shows theoretical results and purple squares indicate simulation results) and propagation length (solid red line shows theoretical results and circles indicate simulation results) of the symmetric waveguide (a) with slot width for a metal thickness of 200 nm and (b) with metal thickness for a slot width of 20 nm.

shows the theoretical values of propagation length calculated by the expression $1/2[\text{Imag}(n_{\text{mode}}k_0) + \alpha]$. Here, α accounts for the absorption taking place during reflection computed from the following equation:

$$\exp\left(-2\alpha \times l \times \tan\theta\right) = |r_1 r_2| \tag{13}$$

$2 \times l \times \tan\theta$ is the path covered in a single roundtrip along the mode propagation direction ($y-$direction). The red circles in Figure 5a show the propagation length values gathered from the simulations. Figure 5b shows the variation of the effective index with metal thickness for a slot width of 20 nm. The index values increase with increasing metal thickness and approach n_{MIM} asymptotically as $l \to \infty$. Conversely, the propagation length of the mode becomes shorter.

3.2 Asymmetric Waveguide

Figure 6 shows the total phase for an asymmetric waveguide. The slot dimensions are the same as those presented in Figure 4. The blue solid line represents a total phase of 0 and the red circles represent the modal solutions for the different slot widths. Figure 7a shows the influence of slot width on the fundamental mode index and propagation length of the asymmetric waveguide. Similar to symmetric waveguides, the index increases with decreasing width. However, unlike a symmetric waveguide, it does not always sustain a bound mode for any combination of source and waveguide parameters. Figure 7b shows the variation of mode index with the height of metal film for a gap of 30 nm. The effective index increases with an increase in width and approaches n_{MIM} for $l \to \infty$ similar to the symmetric waveguide.

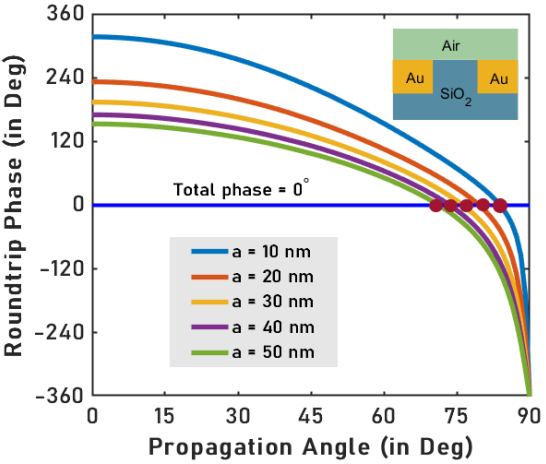

Fig. 6 Total roundtrip phase of the EM waves in the asymmetric waveguide with SiO_2 inside and below it and air above it, for widths of 10 nm to 50 nm and metal thickness of 200 nm. Horizontal blue line represents a total phase of 0 and red circles are fundamental mode solutions.

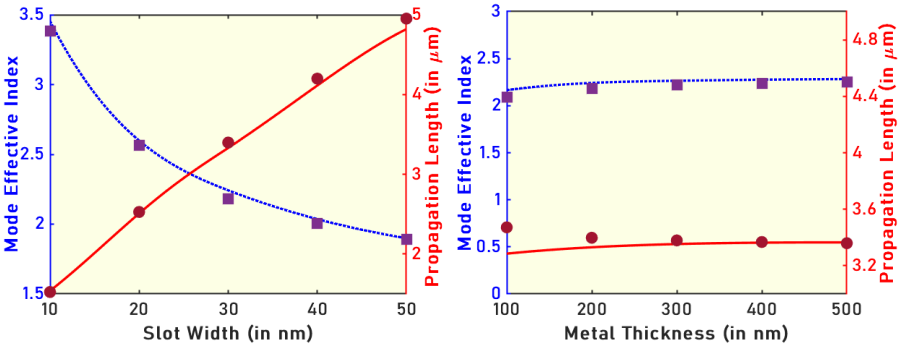

(a) (b)

Fig. 7 Variation of the fundamental mode effective index (blue dotted line shows theoretical results and purple squares indicate simulation results) and propagation length (red solid line shows theoretical results and circles indicate simulation results) of the asymmetric waveguide (a) with slot width for a metal thickness of 200 nm and (b) with metal thickness for a slot width of 30 nm.

It is important to note that the theory is most accurate in the fundamental mode calculation when the slot's aspect ratio (ratio of metal thickness to slot width) is greater than 1. Previous work has shown that the gap plasmon mode no longer remains the fundamental mode for lower aspect ratio slots, as a result, the quasi-TEM condition does not hold [26]. The gap plasmon formulation of the plasmonic slot waveguide should therefore be used for $l > a$.

3.3 Higher Order Modes

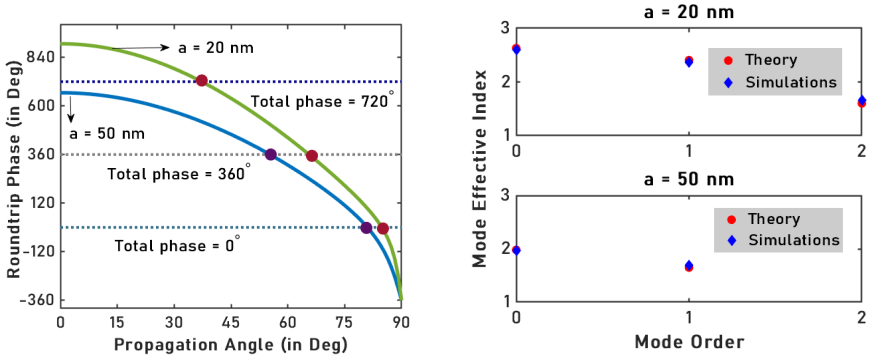

(a) (b)

Fig. 8 (a) Fundamental and higher order modal solutions for an asymmetric waveguide of thickness 750 nm and widths 20 nm and 50 nm. Horizontal dotted lines indicate a phase of 0°, 360°, and 720°. (b) Mode effective indices of the above orders from theoretical calculations and numerical simulations

Although single-mode operation is desired for most applications of plasmonic slot waveguides, we believe it is useful to validate our analysis for higher-order modes as well. We use an asymmetric waveguide with the same configuration as in Section 3.3 for a slot width of 20 nm and an increased thickness of 750 nm. As shown in Figure 8a we obtain zeroth order mode at an angle of 84.8°, 1st order mode at 65.61°, and 2nd order mode at 37.311° marked by the red circles. The corresponding effective indices are calculated from Eq. 12 as 2.6308, 2.4060, and 1.6012 shown in Figure 8b along with the numerical values for the same configuration.

We observe that the presence of higher-order modes (in the $z-$ direction) depends not just on the film thickness but also on the slot width. When the width of the slot is changed from 20 nm to 50 nm, keeping the thickness constant at 750 nm, the number of modes reduces from three to two as indicated in Figure 8a. Their effective indices obtained from theory and numerical calculations are shown in Figure 8b. The number of modes in the slot (localized in the $z-$ direction) and their corresponding index values increase with an increase in the aspect ratio of the slot.

4 Discussion

The theoretical analysis of plasmonic slot waveguides has been done by several works using two main approaches: numerical analysis [1–3, 18, 19, 30] and effective index method (EIM) [49]. Though accurate, numerical simulations lack insight into the physics of mode propagation and are time-consuming. In contrast, the proposed analytical method determines mode properties in

terms of other physical parameters. We used standard numerical integration of Eq. 10; however, approximate solutions to this equation may be attempted [40] (although we have not found them in this work). Compared to the results of a commercially available finite-difference software, we found that the numerical integration we used was two orders of magnitude faster, while the accuracy was within 3%. The accuracy of the simulations was confirmed by a convergence study.

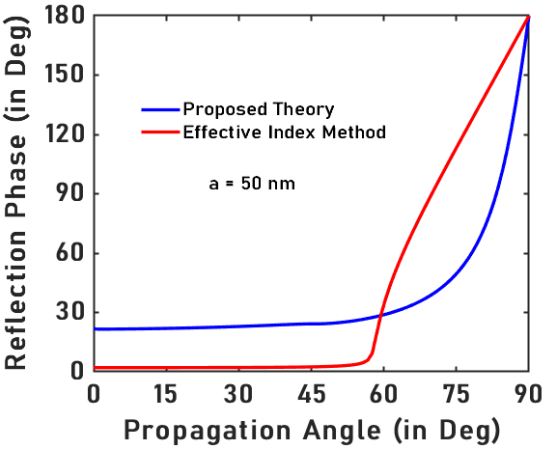

Fig. 9 Reflection phase in a slot of width 50 nm, completely surrounded by SiO_2. The red line represents the phase values calculated using the effective index method and the blue line represents the values obtained from Eq. 10 of the proposed analysis.

The main advantage of the presented approach is that it allows for the efficient design of plasmonic slot waveguides while being more accurate than the analytic effective index approaches. This is because the phase of reflection is different when calculated using the EIM which does not incorporate mode-shape mismatch effects. We have shown the difference between the phase of reflection (for a 50 nm slot) obtained from EIM and the proposed analysis in Figure 9. This is valuable for practical applications where waveguide dispersion, propagation length, and refractive index sensitivity are all more accurately calculated with the analytic approach presented here (as compared to the EIM), while not requiring time-consuming full numerical simulations that lack physical insight. For example, the propagation length is critical for photonic modulators since it provides the on-chip photon loss, and this is found to be significantly more accurate than EIM-based calculations, as shown in Figure 10. For the dimensions studied here, and assuming that the length of a plasmon-based device is limited by the propagation length, we obtained capacitance $\left(\frac{\epsilon \times l_p \times l}{a}\right)$ values of the order of fF (where ϵ is the absolute

permittivity of the MIM region and l_p is the propagation length of the fundamental mode). This means the characteristic time is of the order of tens to a few hundreds of femtoseconds for 50 Ω resistance so it is unlikely to limit the bandwidth in modulation applications.

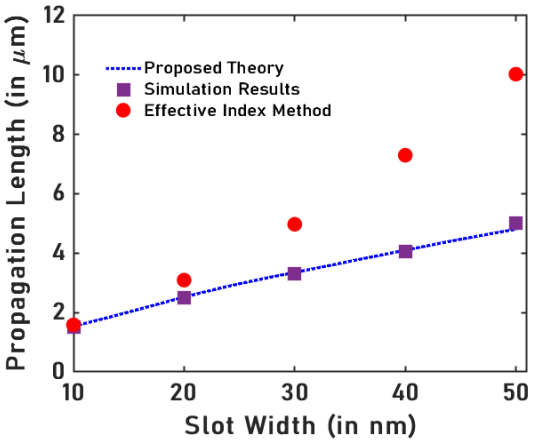

Fig. 10 Propagation length of the fundamental order mode in a symmetric plasmonic slot waveguide of metal height 200 nm, surrounded by SiO_2. The blue dotted line represents the results of the proposed analytic method, the purple squares correspond to the numerical simulations, and the red circles represent the values calculated using the effective index method.

Information about critical propagation angles is an important feature of the model. Both reflectivity and critical angles are dependent on the refractive index of the dielectric in the slot. The changes in the critical angle can therefore be mapped to changes in the refractive index of the slot, which has been shown to be useful in sensing applications using dielectrics [52]. The strong dependence of the reflection phase on the propagation angles, shown in Figures 5b and 7b can also be applied to improve the sensitivity of surface plasmon resonance sensors. We calculated the sensitivity to a 10% and 50% increase in the refractive index of the gap region (silica, 1.44), as shown in Figure 11. Here, the sensitivity was expressed as the absolute change in the mode effective index (Δn_{mode}) of the slot in response to the refractive index changes.

The theory can include the gain of an amplified material in the slot providing a way to analyze the slot geometry for lasing applications [53]. Surface roughness can also play a critical role in device performance [54] and there has been recent work considering the impact in ultra-narrow gaps numerically [55]. It is possible that the present approach can be extended to include surface roughness by adding a surface roughness parameter in the future. At present, the approach works only with the rectangular slot geometry; however, past works have generalized the single mode matching to continuum

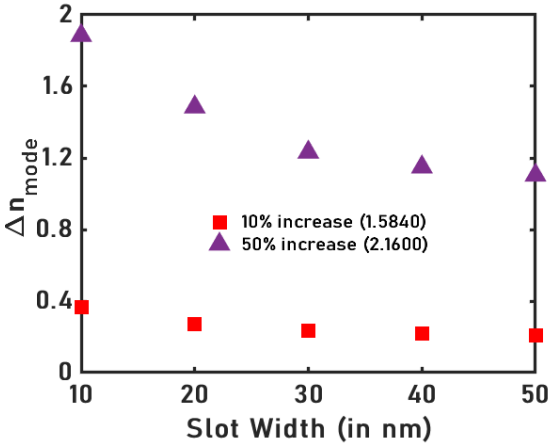

Fig. 11 Absolute change in the mode effective index of the fundamental order mode in a symmetric plasmonic slot waveguide of metal height 200 nm, surrounded by SiO_2, when the refractive index inside the slot is increased by 10% and 50%.

to other geometries and it is possible that the perfect electric conductor approximation used here may also be extended for rapid calculation in those geometries [46, 56]. Although the proposed framework is more accurate than the effective index method and more efficient than numerical simulations, its accuracy sees a decline for extremely narrow gaps or for permittivities where there is significant field penetration into the metal. A larger proportion of the electric field entering the metals reduces the validity of the PEC approximation, limiting the model's accuracy in these scenarios.

5 Conclusion

In conclusion, we presented a fully analytic approach to determine the propagation properties in a 3D plasmonic slot waveguide. We derived an analytic expression for reflection at the slot's interfaces with surrounding media for different propagation angles by using PEC approximation, dielectric loading, and single-mode matching to continuum. The reflection phase values above the critical angles were substituted in the waveguide self-consistency condition to obtain values of propagation angles that supported fundamental and/or higher-order modes. The angular solutions were then used to compute modal properties such as effective index and propagation length for different waveguide parameters. The theoretical results demonstrated close agreement with numerical simulation results, to within 3%. With a growing focus on the miniaturization of circuits and devices across different areas, our approach will be a useful tool for the rapid design and optimization of plasmonic slot geometries with enhanced physical intuition.

Declarations

Funding

Natural Sciences and Engineering Research Council of Canada (CREATE in Quantum Computing Program, Grant Number 543245 and RGPIN-2017-03830).

Conflict of interest/Competing interests

The authors declare no conflicts of interest.

Ethics Approval

Not applicable

Consent to participate

Not applicable

Consent for publication

Not applicable

Availability of data and materials

Data underlying the results presented in this paper are not publicly available at this time but may be obtained from the authors upon reasonable request.

Code availability

MATLAB code can be made available at reasonable request.

Authors' contributions

AP derived the equations, performed the simulations, and wrote the manuscript. RG formulated the theory and wrote the manuscript.

References

[1] Veronis, G., Fan, S.: Guided subwavelength plasmonic mode supported by a slot in a thin metal film. Opt. Lett. **30**(24), 3359–3361 (2005). https://doi.org/10.1364/OL.30.003359

[2] Pile, D.F., Ogawa, T., Gramotnev, D.K., Matsuzaki, Y., Vernon, K.C., Yamaguchi, K., Okamoto, T., Haraguchi, M., Fukui, M.: Two-dimensionally localized modes of a nanoscale gap plasmon waveguide. Appl. Phys. Lett. **87**(26), 261114 (2005). https://doi.org/10.1063/1.2149971

[3] Veronis, G., Fan, S.: Modes of subwavelength plasmonic slot waveguides. Journal of Lightwave Technology **25**(9), 2511–2521 (2007). https://doi.org/10.1109/JLT.2007.903544

[4] Chen, L., Shakya, J., Lipson, M.: Subwavelength confinement in an integrated metal slot waveguide on silicon. Opt. Lett. **31**(14), 2133–2135 (2006). https://doi.org/10.1364/OL.31.002133

[5] Ginzburg, P., Arbel, D., Orenstein, M.: Gap plasmon polariton structure for very efficient microscale-to-nanoscale interfacing. Opt. Lett. **31**(22), 3288–3290 (2006). https://doi.org/10.1364/OL.31.003288

[6] Feng, N.-N., Dal Negro, L.: Plasmon mode transformation in modulated-index metal-dielectric slot waveguides. Opt. Lett. **32**(21), 3086–3088 (2007). https://doi.org/10.1364/OL.32.003086

[7] Tian, J., Yu, S., Yan, W., Qiu, M.: Broadband high-efficiency surface-plasmon-polariton coupler with silicon-metal interface. Appl. Phys. Lett. **95**(1), 013504 (2009). https://doi.org/10.1063/1.3168653

[8] Ono, M., Taniyama, H., Xu, H., Tsunekawa, M., Kuramochi, E., Nozaki, K., Notomi, M.: Deep-subwavelength plasmonic mode converter with large size reduction for Si-wire waveguide. Optica **3**(9), 999–1005 (2016). https://doi.org/10.1364/OPTICA.3.000999

[9] Salamin, Y., Heni, W., Haffner, C., Fedoryshyn, Y., Hoessbacher, C., Bonjour, R., Zahner, M., Hillerkuss, D., Leuchtmann, P., Elder, D.L., Dalton, L.R., Hafner, C., Leuthold, J.: Direct conversion of free space millimeter waves to optical domain by plasmonic modulator antenna. Nano Lett. **15**(12), 8342–8346 (2015). https://doi.org/10.1021/acs.nanolett.5b04025

[10] Melikyan, A., Alloatti, L., Muslija, A., Hillerkuss, D., Schindler, P.C., Li, J., Palmer, R., Korn, D., Muehlbrandt, S., Van Thourhout, D., Chen, B., Dinu, R., Sommer, M., Koos, C., Kohl, M., Freude, W., Leuthold, J.: High-speed plasmonic phase modulators. Nature Photon **8**(3), 229–233 (2014). https://doi.org/10.1038/nphoton.2014.9

[11] Haffner, C., Heni, W., Fedoryshyn, Y., Niegemann, J., Melikyan, A., Elder, D.L., Baeuerle, B., Salamin, Y., Josten, A., Koch, U., Hoessbacher, C., Ducry, F., Juchli, L., Emboras, A., Hillerkuss, D., Kohl, M., Dalton, L.R., Hafner, C., Leuthold, J.: All-plasmonic Mach – Zehnder modulator enabling optical high-speed communication at the microscale. Nature Photon **9**(8), 525–528 (2015). https://doi.org/10.1038/nphoton.2015.127

[12] Haffner, C., Chelladurai, D., Fedoryshyn, Y., Josten, A., Baeuerle, B., Heni, W., Watanabe, T., Cui, T., Cheng, B., Saha, S., Elder, D.L., Dalton, L.R., Boltasseva, A., Shalaev, V.M., Kinsey, N., Leuthold, J.:

Low-loss plasmon-assisted electro-optic modulator. Nature **556**(7702), 483–486 (2018). https://doi.org/10.1038/s41586-018-0031-4

[13] Messner, A., Jud, P.A., Winiger, J., Eppenberger, M., Chelladurai, D., Heni, W., Baeuerle, B., Koch, U., Ma, P., Haffner, C., Xu, H., Elder, D.L., Dalton, L.R., Smajic, J., Leuthold, J.: Broadband metallic fiber-to-chip couplers and a low-complexity integrated plasmonic platform. Nano Lett. **21**(11), 4539–4545 (2021). https://doi.org/10.1021/acs.nanolett.0c05069

[14] Li, S., Zuo, G., Wu, N., Yang, Z., Zhao, B., Xia, L., Li, W.: Hybrid plasmonic nanofocusing waveguide for on-chip sers tweezer. Optics & Laser Technology **143**, 107259 (2021). https://doi.org/10.1016/j.optlastec.2021.107259

[15] Tsai, W.-Y., Huang, J.-S., Huang, C.-B.: Selective trapping or rotation of isotropic dielectric microparticles by optical near field in a plasmonic archimedes spiral. Nano Lett. **14**(2), 547–552 (2014). https://doi.org/10.1021/nl403608a

[16] Choo, H., Kim, M.-K., Staffaroni, M., Seok, T.J., Bokor, J., Cabrini, S., Schuck, P.J., Wu, M.C., Yablonovitch, E.: Nanofocusing in a metal–insulator–metal gap plasmon waveguide with a three-dimensional linear taper. Nature Photon **6**(12), 838–844 (2012). https://doi.org/10.1038/nphoton.2012.277

[17] Heydari, M., Habibzadeh-Sharif, A., Jabbarzadeh, F.: Design of a compact refractive-index sensor based on surface plasmon polariton slot waveguide. Photonics and Nanostructures - Fundamentals and Applications **38**, 100755 (2020). https://doi.org/10.1016/j.photonics.2019.100755

[18] Feng, N.-N., Brongersma, M.L., Dal Negro, L.: Metal–dielectric slot-waveguide structures for the propagation of surface plasmon polaritons at 1.55μm. IEEE Journal of Quantum Electronics **43**(6), 479–485 (2007). https://doi.org/10.1109/JQE.2007.897913

[19] Liu, L., Han, Z., He, S.: Novel surface plasmon waveguide for high integration. Opt. Express **13**(17), 6645–6650 (2005). https://doi.org/10.1364/OPEX.13.006645

[20] Fang, Y., Sun, M.: Nanoplasmonic waveguides: towards applications in integrated nanophotonic circuits. Light Sci Appl **4**(6), 294–294 (2015). https://doi.org/10.1038/lsa.2015.67

[21] Neutens, P., Van Dorpe, P., De Vlaminck, I., Lagae, L., Borghs, G.: Electrical detection of confined gap plasmons in metal–insulator–metal waveguides. Nature Photon **3**(5), 283–286 (2009). https://doi.org/10.

1038/nphoton.2009.47

[22] Zhu, S., Lo, G., Kwong, D.: Theoretical investigation of silicide schottky barrier detector integrated in horizontal metal-insulator-silicon-insulator-metal nanoplasmonic slot waveguide. Opt. Express **19**(17), 15843–15854 (2011). https://doi.org/10.1364/OE.19.015843

[23] Blauth, M., Harms, J., Prechtl, M., Finley, J., Kaniber, M.: Enhanced optical activity of atomically thin $MoSe_2$ proximal to nanoscale plasmonic slot-waveguides. 2D Mat. **4**(2), 021011 (2017). https://doi.org/10.1088/2053-1583/aa52b0

[24] Gordon, R., Dobinson, M.: Plasmonics–mine the gap: opinion. Opt. Mater. Express **11**(7), 2192–2196 (2021). https://doi.org/10.1364/OME.430547

[25] Ozbay, E.: Plasmonics: merging photonics and electronics at nanoscale dimensions. Science **311**(5758), 189–193 (2006). https://doi.org/10.1126/science.1114849

[26] Han, Z., Bozhevolnyi, S.I.: Radiation guiding with surface plasmon polaritons. Reports on Progress in Physics **76**(1), 016402 (2012). https://doi.org/10.1088/0034-4885/76/1/016402

[27] Salamin, Y., Baeuerle, B., Heni, W., Abrecht, F.C., Josten, A., Fedoryshyn, Y., Haffner, C., Bonjour, R., Watanabe, T., Burla, M., Elder, D.L., Dalton, L.R., Leuthold, J.: Microwave plasmonic mixer in a transparent fibre–wireless link. Nature Photon **12**(12), 749–753 (2018). https://doi.org/10.1038/s41566-018-0281-6

[28] Heni, W., Fedoryshyn, Y., Baeuerle, B., Josten, A., Hoessbacher, C.B., Messner, A., Haffner, C., Watanabe, T., Salamin, Y., Koch, U., Elder, D.L., Dalton, L.R., Leuthold, J.: Plasmonic IQ modulators with attojoule per bit electrical energy consumption. Nat Commun **10**(1), 1–8 (2019). https://doi.org/10.1038/s41467-019-09724-7

[29] Ummethala, S., Harter, T., Koehnle, K., Li, Z., Muehlbrandt, S., Kutuvantavida, Y., Kemal, J., Marin-Palomo, P., Schaefer, J., Tessmann, A., Garlapati, S.K., Bacher, A., Hahn, L., Walther, M., Zwick, T., Randel, S., Freude, W., Koos, C.: Thz-to-optical conversion in wireless communications using an ultra-broadband plasmonic modulator. Nat. Photonics **13**(8), 519–524 (2019). https://doi.org/10.1038/s41566-019-0475-6

[30] Dionne, J., Sweatlock, L., Atwater, H., Polman, A.: Plasmon slot waveguides: Towards chip-scale propagation with subwavelength-scale localization. Phys. Rev. B **73**(3), 035407 (2006). https://doi.org/10.1103/PhysRevB.73.035407

[31] Takakura, Y.: Optical resonance in a narrow slit in a thick metallic screen. Phys. Rev. Lett. **86**(24), 5601 (2001). https://doi.org/10.1103/PhysRevLett.86.5601

[32] Yang, F., Sambles, J.R.: Resonant transmission of microwaves through a narrow metallic slit. Phys. Rev. Lett. **89**(6), 063901 (2002). https://doi.org/10.1103/PhysRevLett.89.063901

[33] Bravo-Abad, J., García-Vidal, F., Martín-Moreno, L.: Resonant transmission of light through finite chains of subwavelength holes in a metallic film. Phys. Rev. Lett. **93**(22), 227401 (2004). https://doi.org/10.1103/PhysRevLett.93.227401

[34] Shin, H., Yanik, M.F., Fan, S., Zia, R., Brongersma, M.L.: Omnidirectional resonance in a metal–dielectric–metal geometry. Appl. Phys. Lett. **84**(22), 4421–4423 (2004). https://doi.org/10.1063/1.1758306

[35] Zia, R., Chandran, A., Brongersma, M.L.: Dielectric waveguide model for guided surface polaritons. Opt. Lett. **30**(12), 1473–1475 (2005). https://doi.org/10.1364/OL.30.001473

[36] Garcia-Vidal, F., Moreno, E., Porto, J., Martin-Moreno, L.: Transmission of light through a single rectangular hole. Phys. Rev. Lett. **95**(10), 103901 (2005). https://doi.org/10.1103/PhysRevLett.95.103901

[37] De Abajo, F.G., Gómez-Medina, R., Sáenz, J.: Full transmission through perfect-conductor subwavelength hole arrays. Phys. Rev. E **72**(1), 016608 (2005). https://doi.org/10.1103/PhysRevE.72.016608

[38] García-Vidal, F., Martín-Moreno, L., Moreno, E., Kumar, L., Gordon, R.: Transmission of light through a single rectangular hole in a real metal. Phys. Rev. B **74**(15), 153411 (2006). https://doi.org/10.1103/PhysRevB.74.153411

[39] Gordon, R.: Light in a subwavelength slit in a metal: propagation and reflection. Phys. Rev. B **73**(15), 153405 (2006). https://doi.org/10.1103/PhysRevB.73.153405

[40] Gordon, R.: Angle-dependent optical transmission through a narrow slit in a thick metal film. Phys. Rev. B **75**(19), 193401 (2007). https://doi.org/10.1103/PhysRevB.75.193401

[41] Eftekhari, F., Gordon, R.: Geometric optics method for surface plasmon integrated circuits. Opt. Express **15**(18), 11595–11600 (2007). https://doi.org/10.1364/OE.15.011595

[42] Mary, A., Rodrigo, S.G., Martin-Moreno, L., Garcia-Vidal, F.: Theory of

light transmission through an array of rectangular holes. Phys. Rev. B **76**(19), 195414 (2007). https://doi.org/10.1103/PhysRevB.76.195414

[43] Christensen, J., Martin-Moreno, L., Garcia-Vidal, F.J.: Theory of resonant acoustic transmission through subwavelength apertures. Phys. Rev. Lett. **101**(1), 014301 (2008). https://doi.org/10.1103/PhysRevLett.101.014301

[44] Barnard, E.S., White, J.S., Chandran, A., Brongersma, M.L.: Spectral properties of plasmonic resonator antennas. Opt. Express **16**(21), 16529–16537 (2008). https://doi.org/10.1364/OE.16.016529

[45] White, J.S., Veronis, G., Yu, Z., Barnard, E.S., Chandran, A., Fan, S., Brongersma, M.L.: Extraordinary optical absorption through subwavelength slits. Opt. Lett. **34**(5), 686–688 (2009). https://doi.org/10.1364/OL.34.000686

[46] Gordon, R.: Reflection of cylindrical surface waves. Opt. Express **17**(21), 18621–18629 (2009)

[47] Verslegers, L., Yu, Z., Catrysse, P.B., Fan, S.: Temporal coupled-mode theory for resonant apertures. J. Opt. Soc. Am. B **27**(10), 1947–1956 (2010). https://doi.org/10.1364/JOSAB.27.001947

[48] Landreman, P.E., Chalabi, H., Park, J., Brongersma, M.L.: Fabry-perot description for mie resonances of rectangular dielectric nanowire optical resonators. Opt. Express **24**(26), 29760–29772 (2016). https://doi.org/10.1364/OE.24.029760

[49] Bozhevolnyi, S.I.: Effective-index modeling of channel plasmon polaritons. Opt. Express **14**(20), 9467–9476 (2006). https://doi.org/10.1364/OE.14.009467

[50] Johnson, P.B., Christy, R.-W.: Optical constants of the noble metals. Phys. Rev. B **6**(12), 4370 (1972). https://doi.org/10.1103/PhysRevB.6.4370

[51] Pati, A., Gordon, R.: Maximum power transfer in a real metal slit: an analytic approach. Opt. Express **29**(23), 38129–38139 (2021). https://doi.org/10.1364/OE.442326

[52] Ma, G., Liang, R., Wan, Z., Wang, S.: Critical angle reflection imaging for quantification of molecular interactions on glass surface. Nat Commun **12**(1), 1–9 (2021). https://doi.org/10.1038/s41467-021-23730-8

[53] Smalley, J.S., Vallini, F., Gu, Q., Fainman, Y.: Amplification and lasing of plasmonic modes. Proceedings of the IEEE **104**(12), 2323–2337 (2016).

https://doi.org/10.1109/JPROC.2016.2582078

[54] Ciracì, C., Vidal-Codina, F., Yoo, D., Peraire, J., Oh, S.-H., Smith, D.R.: Impact of surface roughness in nanogap plasmonic systems. ACS Photonics **7**(4), 908–913 (2020). https://doi.org/10.1021/acsphotonics.0c00099

[55] Treebupachatsakul, T., Shinnakerdchoke, S., Pechprasarn, S.: Analysis of effects of surface roughness on sensing performance of surface plasmon resonance detection for refractive index sensing application. Sensors **21**(18), 6164 (2021). https://doi.org/10.3390/s21186164

[56] Min, Q., Gordon, R.: Squeezing light into subwavelength metallic tapers: single mode matching method. J. Nanophoton. **3**(1), 033505 (2009). https://doi.org/10.1117/1.3204944